# MitoStructSeg: A Comprehensive Platform for Mitochondrial Structure Segmentation and Analysis

Xinsheng Wang[1], Buqing Cai[1], Zhuo Jia[1], Yuanbo Chen[1], Shuai Guo[2], Zheng Liu[2], Fuwei Li[1], Hao Dong[1], Fa Zhang[1*], Xiaohua Wan[1*], Bin Hu[1*]
[1]Beijing Institute of Technology, Beijing, China
[2] Southern University of Science and Technology, Shenzhen, China

Mitochondria are vital organelles within cells, playing key roles in energy conversion, cell death, and signal transduction. Structurally, mitochondria consist of outer membrane and inner cristae, with the latter being critical for energy production. Quantitative analysis of the inner cristae provides insights into mitochondrial function, cellular metabolism, and pathological conditions. However, the complex mitochondrial architecture, along with challenges such as sample preparation noise and imaging interference, limits the effectiveness of current analytical tools. In this study, we introduce MitoStructSeg, a deep learning-based platform for mitochondrial structure segmentation and quantitative analysis. At its core, we propose AMM-Seg, a robust model specifically designed to segment key mitochondrial structures, including the outer membrane and inner cristae. Furthermore, MitoStructSeg includes an automated quantitative analysis module that extracts key morphological metrics, such as surface area, volume, and cristae density. This enables comprehensive and efficient assessments of mitochondrial morphology, supporting both basic research and clinical applications. Additionally, we provide a user-friendly, open-source tool to ensure practical usability.

Mitochondria play a central role in cell biology and are regarded as the powerhouses of the cell[1–3] due to their critical function in energy production. Understanding the structure of mitochondria is essential to unravel the mechanisms that facilitate efficient energy conversion and regulate biological processes[4–7]. Some researches show that in damaged myocardial tissue, the structure of mitochondria in cardiomyocytes undergoes varying degrees of damage[8,9]. The structure of mitochondria primarily consists of two membranes: outer membrane and inner membrane that is folded into cristae. Furthermore, the cristae damage is strongly associated with numerous diseases[10–12], highlighting the importance of detailed studies on mitochondrial structure, especially the cristae structure.

Given mitochondria complex subcellular structure, detailed imaging techniques are required to fully understand mitochondria morphology and function. Scanning electron microscopy (SEM)[13,14] is commonly employed for this purpose, offering high-resolution images of mitochondrial ultrastructure. In particular, focused ion beam scanning electron microscopy (FIB-SEM)[15–18] offers several distinct advantages, allowing for three-dimensional reconstruction with isotropic resolution in the low nanometer range. These capabilities make FIB-SEM particularly effective for examining the fine details of mitochondrial structure. However, the complex and variable morphology of mitochondria[19,20] presents significant challenges for image segmentation[21–26]. The image noise and the variability in mitochondrial size and shape complicate segmentation. Additionally, the intricate folding of the inner membrane and its proximity to the outer membrane, along with the varying shapes and densities of cristae, make accurate segmentation particularly challenging.

The widespread adoption of deep learning technologies across various fields has highlighted its growing potential in biomedical image analysis[27–29]. DeepContact[30] is a UNet-based[31] model designed to segment and analyze membrane contact sites between mitochondria and the ER in electron microscopy images. However, it cannot segment the mitochondrial cristae, preventing the accurate capture of the detailed mitochondrial structure and morphological changes. PHILOW[32] utilizes a HITL-TAP model to automatically segment the topological structure of mitochondrial cristae. However, it requires manual interaction to refine and correct the model's output, limiting its fully automated capability. Moreover, most existing methods primarily focus on generating initial segmentation results and lack quantitative analysis of these results[30,33–35]. Quantitative analysis of mitochondrial information is crucial for understanding their dynamics and alterations in disease contexts, as it provides insights into mitochondrial morphology and health status. To better understand mitochondrial changes during disease progression, there is an urgent need for a tool that can not only accurately segment mitochondrial structure but also provide quantitative analysis of the segmentation outcomes.

To address this problem comprehensively, we have developed MitoStructSeg, the first fully automated platform that both integrates mitochondrial structure segmentation and quantitative analysis. Our platform includes the Adaptive Multi-domain Mitochondrial segmentation module (AMM-Seg), a novel algorithm we designed that automatically segments both the mitochondrial outer membrane and inner cristae. In addition, MitoStructSeg provides advanced tools for quantifying key mitochondrial features such as volume, surface area, and cristae density. Analyzing these results, our platform explores correlations between mitochondrial characteristics and health status, providing valuable insights

into mitochondrial function and pathology. MitoStructSeg has been validated on different samples from specific cell tissue types, revealing intricate details of mitochondrial structure under various physiological conditions.

## Results

### The Design of MitoStructSeg

MitoStructSeg is an integrated platform that automatically segments mitochondrial structures, including the outer membrane and inner cristae, and quantitatively analyzes the segmentation results to identify mitochondrial damage. As shown in the Fig.1, the platform consists of two modules: the mitochondrial structure segmentation module and the mitochondrial quantitative analysis module. The mitochondrial structure segmentation module is based on the Adaptive Multi-domain Mitochondrial segmentation (AMM-Seg) network architecture (Supplementary Fig.1) that we proposed. The mitochondrial quantitative analysis module processes segmentation results to generate quantitative data, including surface area, volume, and cristae density. In addition, we perform 3D visualization[36] of the segmentation results to further illustrate the structural details and highlight the state of mitochondrial damage.

The mitochondrial data are obtained from the myocardial tissues of three COVID-19 patients and are collected using FIB-SEM, with a voxel size of 5 nm $\times$ 5 nm and a slice interval of 10 nm (see Methods Section 1 for more details on the dataset). The AMM-Seg model uses 200 labeled images (800x800 pixels) from Patient#1 dataset as the source domain, while 200 unlabeled images (800x800 pixels) are employed as the target domain for training. The target domain is derived from other datasets to more effectively evaluate the model's generalization ability on different types of dataset. We focus on the data within the red dotted box (800x800x800 voxels) for predictive analysis. Additionally, other methods are also based on the same dataset to evaluate results and make comparisons. The segmentation results of AMM-Seg and Ground Truth are visualized to evaluate the actual effect of segmentation (Fig.2A). We utilize three distinct metrics for evaluation: (1) The degree to which the mitochondrial structure in a predicted domain overlaps with a true domain is measured via the Intersect-over-Union (IoU) between the mitochondrial structure in the predicted and ground-truth domains. (2) The Matthews Correlation Coefficient (MCC) takes into account all four classification outcomes: true positives, false positives, true negatives, and false negatives. The score ranges from -1 to 1, where 1 signifies perfect prediction, 0 indicates random effects, and -1 denotes complete errors. Since the MCC is unaffected by the uneven distribution of samples, it is particularly well-suited for datasets with class imbalances. (3) The F1 score, a harmonic mean of precision and recall, combines precision and recall to assess the model's accuracy in identifying true positives.

We perform an ablation study to analyze the role of each component in the proposed model AMM-Seg. In particular, we have the following variants: (1) w/o augmented image: removing the augmented image and only used the textured image. (2) w/o textured image: similar to w/o augmented Image, only the augmented image are used. (3) w/o adaptive fusion: the image features generated by the augmented image and the textured image are fused in equal weight fusion to replace the adaptive fusion module (See Methods Section 2 for more details on AMM-Seg components). It can be observed from the Fig.2B that when either the augmented or the textured image is removed, the effect on the three datasets decreases. This highlights that the model achieves better performance when both the textured image and the augmented image are applied together, outperforming the use of either one alone. This demonstrates that incorporating texture information can effectively enhance the structural features of the image. Finally, an adaptive fusion strategy is employed to integrate the augmented image and the textured image, yielding results significantly superior to those of the equal weight fusion strategy. This indicates that the integration of adaptive fusion mechanism allows the model to dynamically adjust its focus based on the feature's importance, particularly enhancing its attention towards the structural features of mitochondria. In general, each component contributes to the performance of the proposed model, and their combination shows the best performance.

After validating the effectiveness of the AMM-Seg architecture, we further investigated the impact of optimization strategies on model performance, with a particular focus on learning rate configuration and dynamic scheduling. In deep learning, the learning rate plays a crucial role in determining both the convergence speed and the generalization ability of the model. To ensure robust and stable training, AMM-Seg employs a multi-stage dynamic learning rate schedule, where a specified initial learning rate is progressively reduced using a polynomial decay strategy. This approach allows the model to maintain strong learning capacity during the early training stages while gradually lowering the update rate as training progresses, thereby reducing the risk of overfitting and supporting stable convergence. As illustrated in Fig.2C, we evaluated the model's performance under this dynamic schedule using three different initial learning rates. The results show that the optimal learning rate varies across datasets: 0.0001 yielded the best performance on the Patient#1 dataset, while 0.0005 performed better for Patient#2 and Patient#3. These findings suggest that the optimal initialization of the learning rate is influenced by the specific structural and textural characteristics of each dataset and, ideally, should be selected adaptively. However, in practice, when prior knowledge about the dataset is limited, an initial learning rate of 0.0005 serves as a robust and effective default across diverse data sources. More importantly, our experiments demonstrate that a well-designed dynamic learning rate

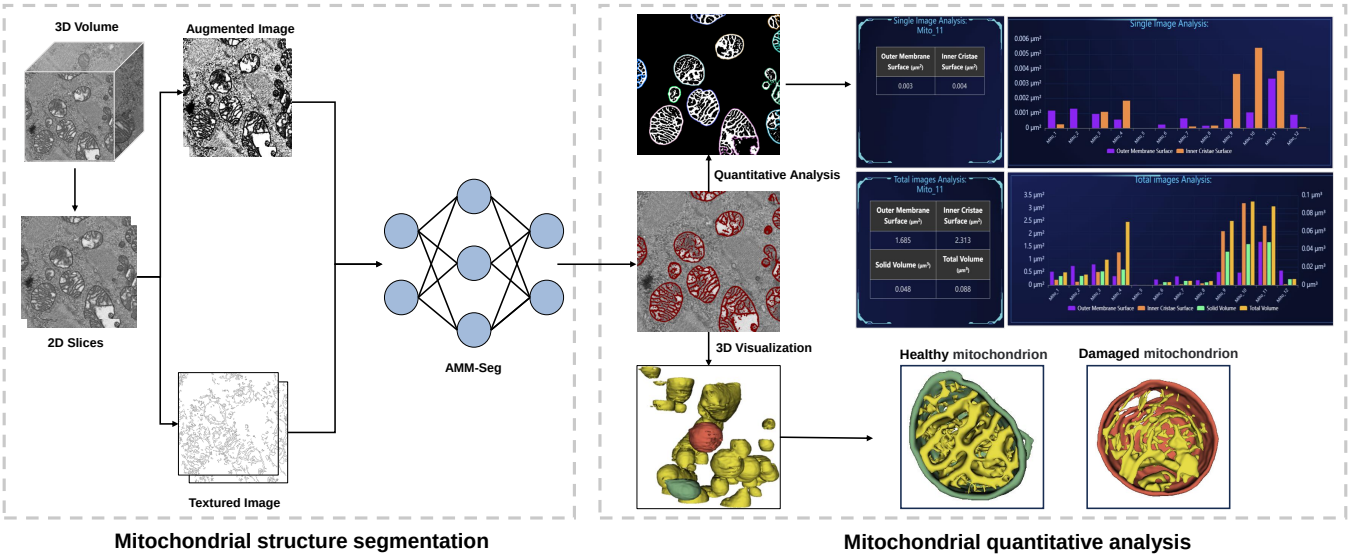


**Fig. 1 The architecture of MitoStructSeg.** MitoStructSeg's workflow includes mitochondrial structure segmentation and mitochondrial quantitative analysis. **Mitochondrial structure segmentation,** First, 3D mitochondrial volume blocks are sliced to generate 2D slices. The 2D slices are then processed to generate augmented images, which enhance feature diversity, and texture images, which provide detailed texture features. The augmented images and texture images are subsequently input into the AMM-Seg, yielding segmentation results of the mitochondrial structure. **Mitochondrial quantitative analysis,** A user-friendly GUI is provided for statistical analysis of the segmentation results, enabling the extraction of key metrics such as surface area, volume, and cristae density. Additionally, we leverage the open-source tool 3D Slicer for visualizing the segmentation results, clearly illustrating the structural differences between healthy and damaged mitochondria.

strategy plays a critical role in enhancing both the accuracy and stability of the segmentation model, highlighting the importance of coupling architectural design with training optimization for improved performance.

### Comparison of mitochondrial structure segmentation with state-of-the-art methods

We conduct a comparative analysis of the segmentation performance of AMM-Seg against five benchmark methods, including MEDIAR[33,34], DA-ISC[35], Unet[31], Swin unetr[37] and Unetr[38]. These benchmark methods utilize advanced segmentation techniques, incorporating multimodal data processing, domain adaptation strategies, and novel neural network architectures to improve accuracy and performance in biomedical image analysis. The segmentation results of each method are visually compared, as illustrated in Fig.3A. The UNet, Swin unetr, and Unetr methods perform the poorest among the methods evaluated. Their segmentation results often fail to capture the complete structure of mitochondria, resulting in sparse and blurred outlines with high false-positive rates. This demonstrates their inability to effectively segment mitochondrial structure, particularly in datasets with highly complex features. The DA-ISC and MEDIAR methods demonstrate noticeable improvements over UNet, Swin Unetr, and Unetr. Their segmentation results are closer to the Ground Truth and manage to capture most structural outlines accurately. However, in regions with intricate inner cristae structures, their performances begin to show limitations, with slight deviations from the true contours. In contrast, AMM-Seg demonstrates superior performance in preserving intricate inner cristae structures, consistently achieving segmentation results that closely align with the Ground Truth. Its red contours closely match the blue contours of the Ground Truth, even in the most structurally complex regions. This demonstrates AMM-Seg's exceptional capability to accurately segment mitochondrial structure and adapt to the complexity of different datasets. Subsequently, to evaluate the effects of all methods more accurately, F1 scores are assessed for the 40 images (800x800 pixels) in the validation set (Fig.3B). The Unet, Swin unetr, and unetr methods exhibit the lowest F1 scores, with values that are highly scattered and show significant fluctuations. This reflects their poor stability and limited ability to handle the variability in mitochondrial structure across different datasets. Although DA-ISC and MEDIAR achieve higher median F1 scores than UNet, Swin Unetr, and Unetr, their results still show fluctuations across different datasets, indicating that there is still a need for improvement in domain adaptation. AMM-Seg outperforms all other methods, achieving the highest median F1 score with minimal fluctuation across the three datasets. This indicates not only its superior

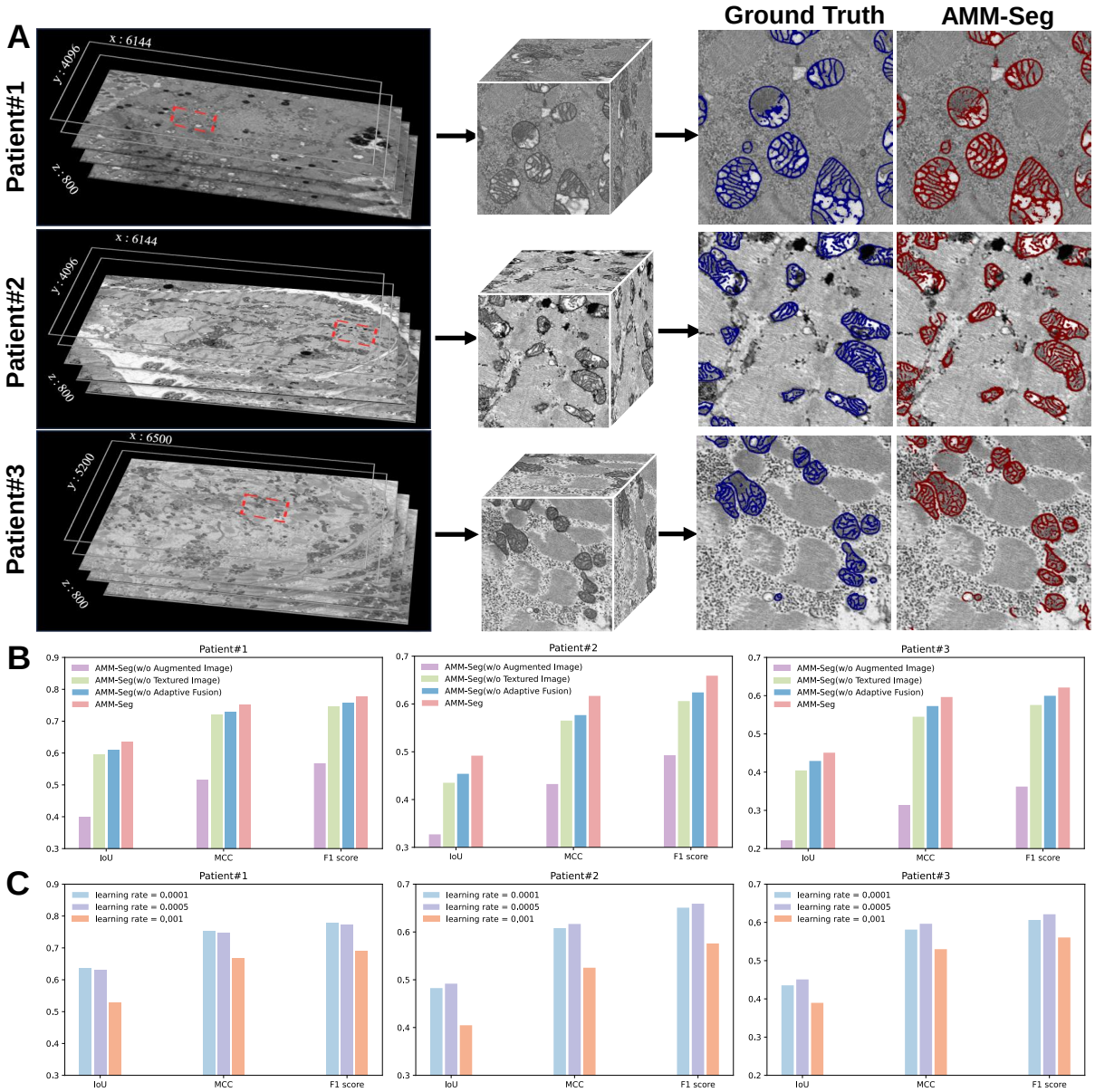


**Fig. 2 The segmentation performance of AMM-Seg in different mitochondrial datasets.** **A,** The image processing and segmentation results of three datasets are shown. The left image of each dataset shows the FIB-SEM acquired data, the middle image shows the cropped area indicated by the red dashed box, and the right image compares the ground truth (blue label) with the segmentation result of the AMM-Seg model (red label). **B,** The results of the ablation experiments for AMM-Seg are presented. The ablation experiment compares the performance of the AMM-Seg without "Augmented Image", "Textured Image", "Adaptive Fusion", and with the complete AMM-Seg methods. **C,** We compared the effects of different learning rates (0.0001, 0.0005, and 0.001) on the segmentation performance of three datasets. The results show that different learning rates have a significant impact on segmentation performance. For Patient#1 dataset, a learning rate of 0.0001 yields the best effect, whereas for Patient#2 and Patient#3 datasets, a learning rate of 0.0005 proves most effective.

segmentation accuracy but also its remarkable stability. The method consistently performs well, regardless of the complexity or variability present in the datasets. It is worth noting that most mitochondrial segmentation tasks currently use block segmentation, which has relatively high overall performance metrics[33–35]. For comparison, we also conduct experiments on the mitochondrial block segmentation task and present the results in Fig.4.

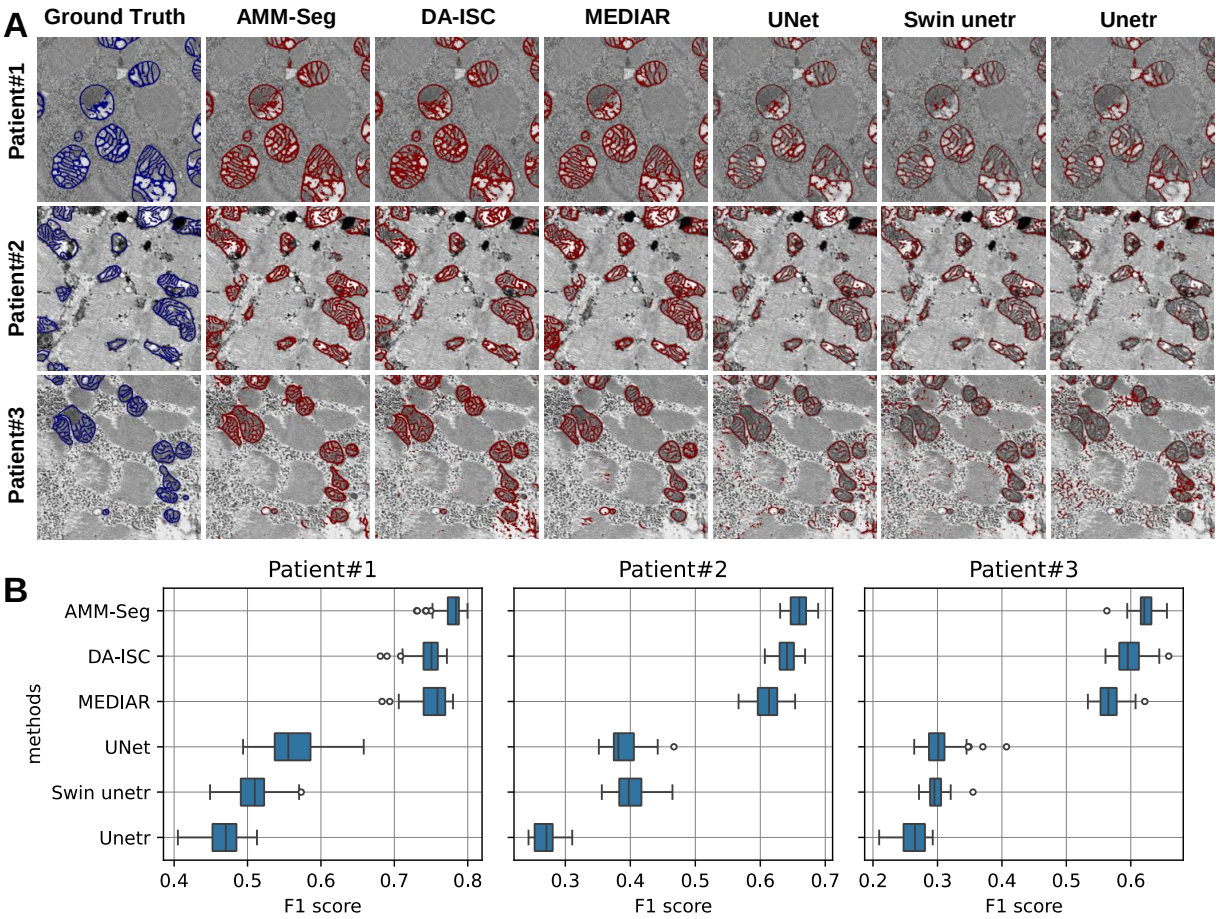


**Fig. 3 Visual and quantitative comparison of AMM-Seg performance with other mainstream methods in mitochondrial structure segmentation task. A,** Unet, Swin Unetr and Unetr perform poorly in the three datasets, producing sparse segmentation results and high false positive rates. The segmentation results of DA-ISC and MEDIAR are relatively close to the true values, but still have some bias when dealing with complex inner cristae structure. In contrast, AMM-Seg method shows superior performance, with its red contours being highly consistent with the ground truth (blue contours), demonstrating an excellent ability to adapt to complex structure. **B,** Quantitative comparison results reveal that the F1 score distributions of the Unet, Swin Unetr, and Unetr methods are relatively scattered, showing large fluctuations and lower medians. The DA-ISC and MEDIAR methods perform better, with scores second only to AMM-Seg. Notably, the AMM-Seg method achieves the highest median and the smallest score fluctuation in F1 scores across the three datasets, demonstrating not only accurate but also highly stable segmentation performance.

Compared to mitochondrial block segmentation, mitochondrial structure segmentation is considerably more challenging, as the structures exhibit fine, line-like features that are highly sensitive to minor segmentation errors. Consequently, mitochondrial structure segmentation task yields relatively lower overall performance metrics.

To verify the model's performance on images with different resolutions, we downsample the original images and then perform segmentation prediction analysis. The experimental steps are as follows: we start with a selected original image and successively reduce it to 1/2 and 1/4 of its original size to simulate different resolution levels. During the image reduction process, we choose the LANCZOS filter[39], which effectively reduces the aliasing effects that may be introduced by the reduction operation. Subsequently, to ensure processing consistency, we use nearest-neighbor interpolation to restore all reduced images to a unified 800x800 pixels resolution. We then use our previously trained model to make segmentation predictions and evaluate its performance across images of varying resolutions. From the results (Supplementary Fig.2), it is observable that although the image details gradually blur due to the reduction in resolution, the prediction output of the model does not show significant degradation. The AMM-Seg continues to ac-

curately identify and segment the outer membrane and inner cristae of mitochondria. This consistency demonstrates the high generalization ability of our model in processing images of different resolutions.

### Comparison of mitochondrial outer membrane and inner cristae segmentation with state-of-the-art methods

The mitochondrial outer membrane is a closed boundary, while the inner cristae are densely packed and exhibit complex morphology. To evaluate the model's segmentation performance on these distinct substructures, we conduct separate experiments for outer membrane and inner cristae segmentation.

The outer membrane segmentation task emphasizes the accurate delineation of smooth, continuous membrane boundaries, which is crucial for evaluating the model's ability to capture fine structural contours. To assess performance on this task, we conduct a comparative analysis from two perspectives: the traditional mitochondrial block segmentation task and a dedicated outer membrane segmentation task. For the AMM-Seg, DA-ISC, and MEDIAR methods, there is no need to retrain the model specifically for mitochondrial block segmentation. Based on the mitochondrial structure segmentation results from the previous step, the segmentation of mitochondrial blocks can be obtained using the Flood Fill method[40]. However, for the UNet, Swin unetr, and Unetr methods, the segmented outer membranes are often fragmented and structurally discontinuous, making the Flood Fill method inapplicable. Consequently, it is necessary to retrain these models specifically for the mitochondrial block segmentation task. The visualization of the mitochondrial block segmentation results is illustrated in Fig.4A, where green represents the correctly segmented areas, red indicates the missed segments, and blue highlights the erroneously segmented areas. The results show that on Patient#1 dataset, most methods successfully segment the mitochondrial blocks. Moreover, on Patient#2 and Patient#3 datasets, AMM-Seg outperforms other methods in terms of missed and incorrect segmentations. In addition, the F1 score is utilized to evaluate the 40 images in the validation set. According to the box plot results in Fig.4B, AMM-Seg achieves the highest performance on the three datasets, especially on Patient#2 and Patient#3 datasets. This demonstrates that AMM-Seg possesses strong cross-domain capabilities, maintaining effective segmentation across diverse datasets. Furthermore, we retrain all models and conduct segmentation experiments specifically on the mitochondrial outer membrane (Supplementary Fig.3). Similarly, AMM-Seg achieves the best performance across all three datasets. It is worth noting that this experiment focuses on the segmentation of the mitochondrial outer membrane, which exhibits line-like structures, resulting in relatively lower overall evaluation metrics. Similarly, AMM-Seg achieves the best performance across all three datasets. Compared to the previous block segmentation results, the overall evaluation metrics for outer membrane segmentation are lower. This difference in evaluation metrics can be attributed to the nature of the segmentation targets. Block segmentation typically involves larger, enclosed mitochondrial regions with relatively stable spatial continuity, where small segmentation inaccuracies have limited impact on overall performance scores. In contrast, outer membrane segmentation targets thin, continuous boundary structures that are highly sensitive to edge integrity, where even slight discontinuities or omissions can cause a significant drop in F1 score.

In the inner cristae segmentation task, the focus is on capturing the complex and irregular morphology of the inner cristae, which presents significant challenges due to their intricate structures and high variability. To evaluate the performance of various segmentation approaches, we restrict the labeling to the inner cristae region and retrain all models for a comparative analysis. To verify the performance of AMM-Seg in the task of inner cristae segmentation, we conduct comparative experiments with a variety of mainstream methods (Supplementary Fig.4). In the Patient#1 dataset, the segmentation results (red area) produced by AMM-Seg align closely with the Ground Truth, particularly in regions with intricate edge details and complex morphology. Overall, AMM-Seg not only accurately segments the inner cristae structure but also minimizes errors and prevents over-segmentation. In contrast, other methods exhibit varying levels of blurriness or false positive. In high-density areas, DA-ISC frequently over-segments, while UNet, Swin unter and Unetr tend to under-segment. Additionally, the distribution of F1 scores shows that AMM-Seg's performance is more concentrated, indicating its stability across the three datasets. In contrast, the F1 score distributions for the other methods are more scattered, suggesting their relatively lower robustness across different datasets. The inner cristae typically exhibit intricate and fine texture features in electron microscope images, presenting challenges for precise segmentation. AMM-Seg employs a dual-channel strategy that extracts augmented and textured images to enhance structural features. Additionally, an adaptive fusion strategy dynamically optimizes the selection of structural features. Furthermore, a multi-domain adaptive strategy is applied to improve its cross-domain capabilities.

In summary, these findings confirm that AMM-Seg consistently outperforms existing methods in both mitochondrial outer membrane and inner cristae segmentation tasks, demonstrating superior accuracy, stability, and cross-domain capabilities.

### Comparison of mitochondrial structure segmentation continuity in the z-direction

Original data are acquired by scanning electron microscopy imaging, which exhibits a high degree of continuity between adjacent slices. Therefore, when using a neural network model to segment mitochondria, it is essential not only to accurately segment the inner cristae

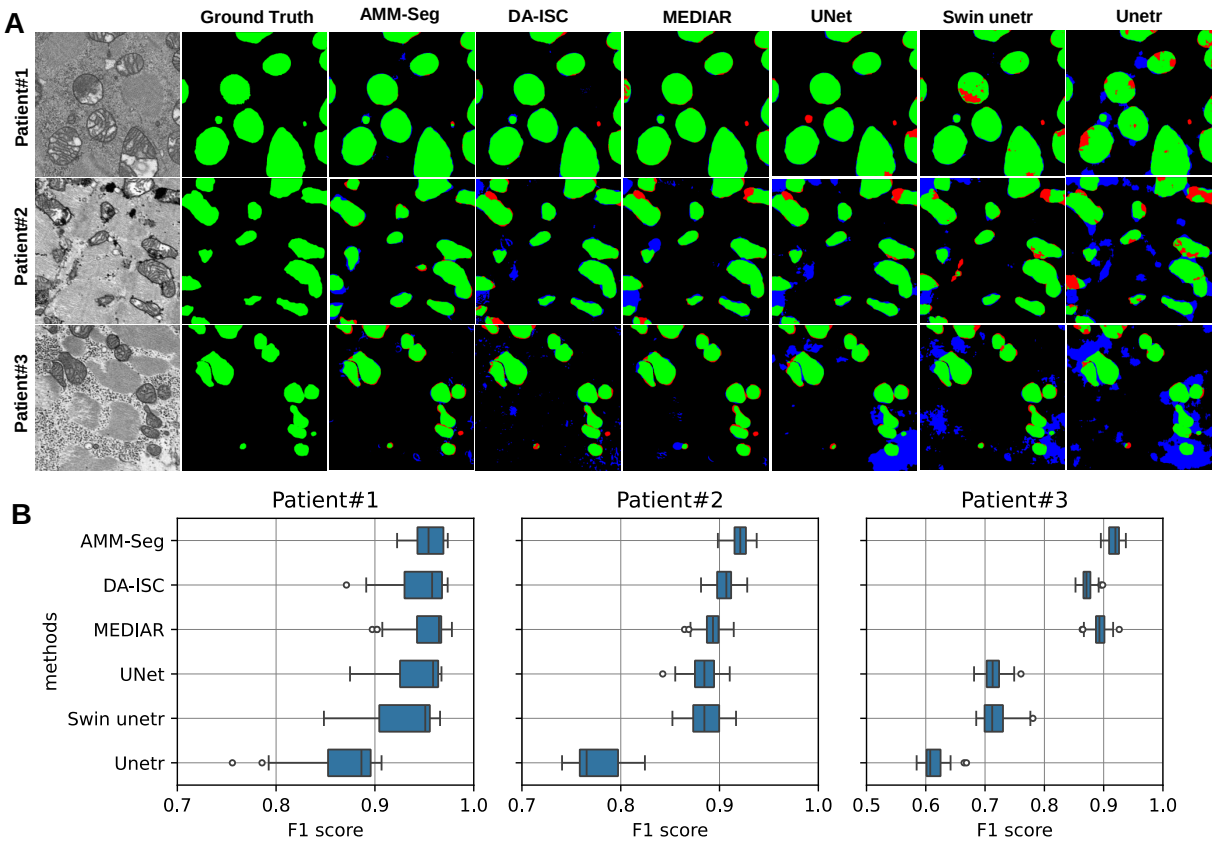


**Fig. 4 Visual and quantitative comparison of AMM-Seg performance with other mainstream methods in mitochondrial block segmentation task.** **A,** The results of AMM-Seg, DA-ISC, and MEDIAR are obtained by Flood Fill based on the mitochondrial structure segmentation results, while UNet, Swin unetr, and unetr are retrained models for block segmentation tasks. From the visualization results, we can observe that in the Patient#1 dataset, the correct part predicted by AMM-Seg (green block) is significantly more consistent with the Ground Truth, and the missing predicted part (red block) and the wrong predicted part (blue block) are significantly fewer than with other methods. In the Patient#2 and Patient#3 datasets, due to the domain adaptation strategy adopted by AMM-Seg, the erroneous segmentation results (blue block) are significantly less than other methods. **B,** In this experiment, we compare the performance of the AMM-Seg F1 score with that of five other methods on three datasets. From the results of the box plot, the overall performance of AMM-Seg, DA-ISC, MEDIAR, and UNet in the Patient#1 dataset is similar, but the performance of AMM-Seg is more stable. In the Patient#2 and Patient#3 datasets, AMM-Seg's performance is significantly better than that of other methods and demonstrates higher stability. This further illustrates the advantage of AMM-Seg in its domain adaptation capabilities.

and outer membranes of mitochondria but also to ensure the continuity of segmentation results between adjacent slices. We select healthy mitochondria from the three datasets for experimental analysis, and the results are shown in Fig.5. Fig.5A shows the 3D visualization of the segmentation results of AMM-Seg and two suboptimal baseline methods (DA-ISC, MEDIAR), with the xz plane intercepted to demonstrate the continuity of the slice segmentation results. A comparison of the three methods reveals that AMM-Seg shows high consistency and integrity in the segmentation results of the three datasets. Especially in the area marked by the red circle, AMM-Seg better maintains the continuity and integrity of the structure, while DA-ISC and MEDIAR exhibit clear segmentation breaks and morphological discontinuities. Fig.5B illustrates the trend of IoU changes among 40 adjacent slices of 800x800 pixels across AMM-Seg and six other segmentation methods (human means manual annotation). The results show that the IoU values of AMM-Seg between slices of three datasets show high stability and continuity, and the IoU fluctuation of AMM-Seg is small, indicating that its segmentation results between slices are more consistent. Especially in the experimental results of Patient#2 and Patient#3, the IoU value of AMM-Seg always remains at a high level in the slice sequence and changes smoothly, which fur-

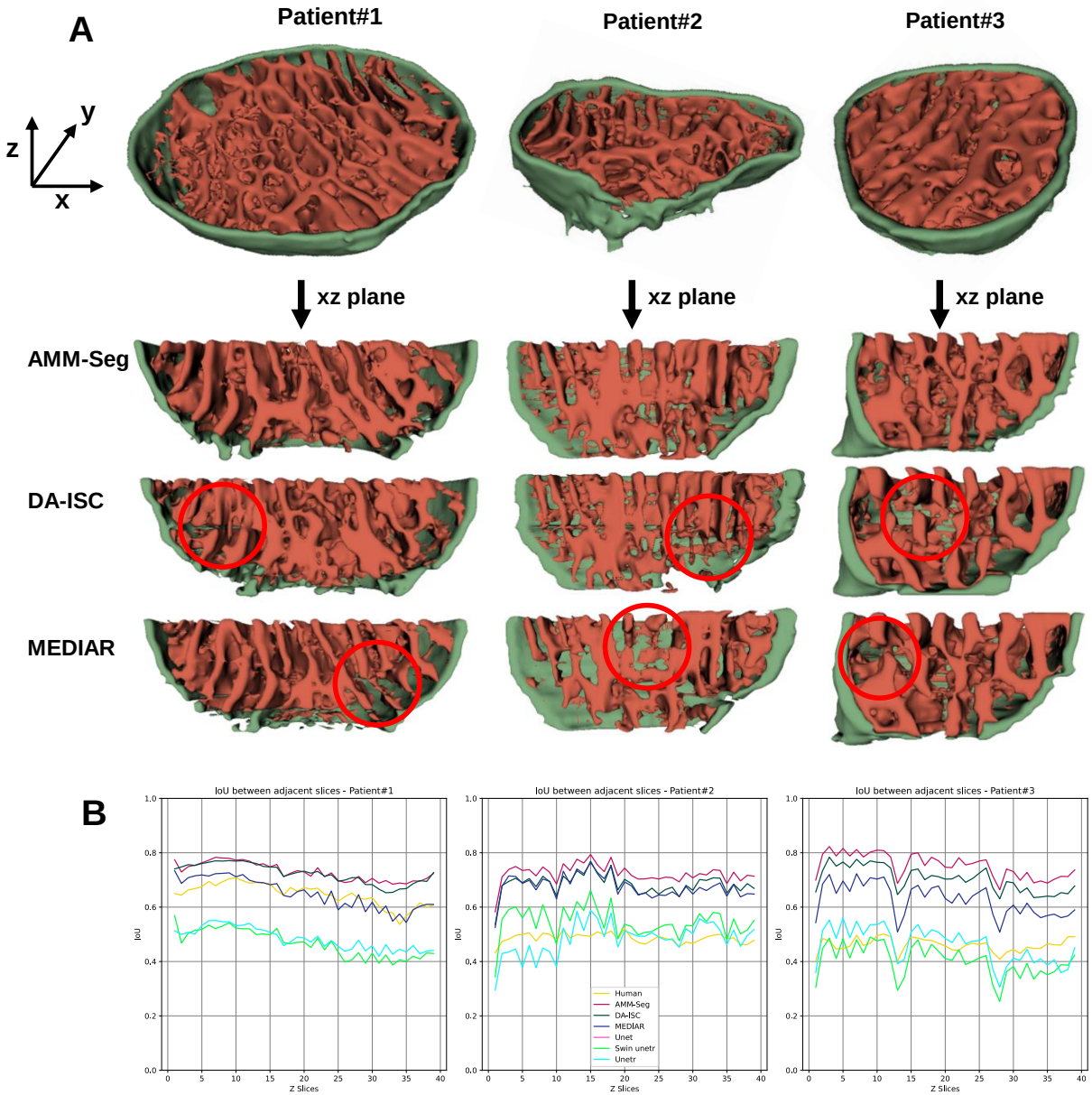


**Fig. 5 Visual and quantitative comparison of 3D reconstruction effects based on segmentation results. A,** The mitochondrial segmentation results of the three datasets are visualized through 3D reconstruction using different segmentation methods (AMM-Seg, DA-ISC, MEDIAR). The xz-plane of the 3D reconstruction is extracted to intuitively compare the differences in 3D reconstruction continuity across methods. The red circles highlight areas with poor segmentation continuity observed in DA-ISC and MEDIAR, while AMM-Seg demonstrates more consistent and accurate results. **B,** IoU Performance Evaluation Between Adjacent Slices. The continuity of 2D image segmentation results is evaluated between adjacent slices for AMM-Seg, six other methods, and human annotation. The IoU curves show that AMM-Seg consistently outperforms DA-ISC, MEDIAR, and other methods across three datasets, maintaining higher IoU values between adjacent slices. These results suggest that AMM-Seg effectively ensures segmentation consistency in the Z-direction through a robust continuity strategy, enabling accurate 3D mitochondrial reconstructions.

ther verifies its advantage of maintaining continuity between slices. The IoU values of methods such as DA-ISC and MEDIAR show a significant decrease and fluctuation in some slices, reflecting that these methods have poor segmentation consistency between slices, which may lead to discontinuity and morphological distortion in the segmentation results. Overall, the AMM-Seg method is significantly better than other methods in terms of 3D structure preservation of segmentation results and continuity between slices. These experimental results show that AMM-Seg can provide more accurate and stable segmentation results, providing a reliable basis for subsequent 3D reconstruction and quantitative analysis.

**Quantitative analysis of mitochondria in healthy and damaged states**

In each of the three datasets, we randomly selected 20 damaged and 60 healthy mitochondria, resulting in a total sample of 240 mitochondria for quantitative analysis. For each mitochondrion, we assess key structural information: the surface area of the outer membrane, the surface area of the inner cristae, the solid volume (including the volume occupied by the outer membrane and inner cristae), and the total volume (the overall volume of the entire mitochondrion). We then calculate three specific ratios for further analysis: the ratio of inner cristae surface area to total volume, represented as $S_{inner}/V_{total}$(Cristae Density[41]), the ratio of inner cristae surface area to outer membrane surface area, represented as $S_{inner}/S_{outer}$ and the ratio of solid volume to total volume, represented as $V_{solid}/V_{total}$. We obtain an 800x800x400 voxel structure segmentation of mitochondria using the AMM-seg method. Given that the original image resolution is 5x5x10 nm per voxel, we downsample the segmentation in the xy plane to produce 400x400x400 voxel block, resulting in a uniform pixel size of 10x10x10 nm. This adjustment provides a consistent scale for real-space representation, facilitating clearer 3D visualization (See Supplentary videos for details).

In Fig.6A, we highlight one healthy mitochondrion in green and one damaged mitochondrion in red, with other mitochondria shown in yellow. The images reveal significant structural differences between healthy and damaged mitochondria: healthy mitochondria exhibit a relatively organized arrangement of inner cristae, while damaged mitochondria show disrupted structure and a disordered cristae arrangement, underscoring the structural changes associated with mitochondrial damage. Secondly, the quantitative statistical results for individual mitochondria are shown in the bottom of Fig.6A. From these results, the $S_{inner}/V_{total}$ (cristae density) values for healthy and damaged mitochondria reveal significant differences between Patient#1 and Patient#3, while the $S_{inner}/S_{outer}$ values demonstrate distinct differences between healthy and damaged mitochondria in Patient#3. Thus, a single statistical result does not provide a definitive distinction between healthy and damaged mitochondria. The results show that the $S_{inner}/V_{total}$ ratios for Health#1, Health#2, and Health#3 are significantly higher than those for Damage#1, Damage#2, and Damage#3. Combined with 3D visualization, it is evident that the more severe the damage to the inner cristae structure in a mitochondrion, the smaller this $S_{inner}/V_{total}$ ratio becomes. This suggests that $S_{inner}/V_{total}$ ratio effectively reflects the cristae density of a mitochondrion, supporting the conclusions of Adams et al.[42]. In contrast, the other two ratios—$S_{inner}/S_{outer}$ and $V_{solid}/V_{total}$—lack consistent trends across datasets and are less effective in distinguishing between healthy and damaged mitochondria. This is primarily because they do not directly capture the architectural complexity of the inner membrane system. The former is sensitive to variations in overall mitochondrial shape, while the latter reflects general structural occupancy without regard to membrane organization. In comparison, $S_{inner}/V_{total}$ quantifies the amount of inner membrane surface per unit volume, serving as a proxy for cristae elaboration and thus mitochondrial bioenergetic potential. This makes it a more sensitive and structurally meaningful indicator of mitochondrial health.

To achieve a more comprehensive analysis of the differences between healthy and damaged mitochondria, we increase our sample size in three datasets. Each dataset includes 20 damaged and 60 healthy mitochondria, resulting in a total of 240 mitochondria. We plot the cumulative distribution curves of healthy mitochondria, damaged mitochondria and all mitochondria on the three datasets, as shown in Fig.6B, Fig.6C and Fig.6D. From the three types of cumulative distribution curves, it is evident that for a given cumulative ratio, the values corresponding to healthy mitochondria are generally higher than damaged mitochondria. This distinction is particularly pronounced in cristae density, where the separation between the distributions of healthy and damaged mitochondria is the most significant, highlighting its effectiveness as a key indicator of mitochondrial health. On the other hand, the volume ratio demonstrates less separation between healthy and damaged mitochondria, indicating that while volume changes may occur during mitochondrial damage, they are less reliable for distinguishing health states. Furthermore, box plots are created with each point representing an individual mitochondrion (Supplementary Fig.5). Additionally, we present statistical data on healthy and damaged mitochondria from the three datasets, each comprising 20 damaged and 60 healthy mitochondria. The analysis includes the maximum, minimum, median, mean, and standard deviation for each property (Supplementary Table 1-3). Overall, these findings emphasize the importance of integrating multiple structural metrics to achieve a more robust and comprehensive evaluation of mitochondrial integrity. To further facilitate the analysis and visualization of these results, we have developed an intuitive and user-friendly interface (Supplementary Fig.6). This interface supports data import, mitochondrial structure segmentation and the preview and analysis of segmenta-

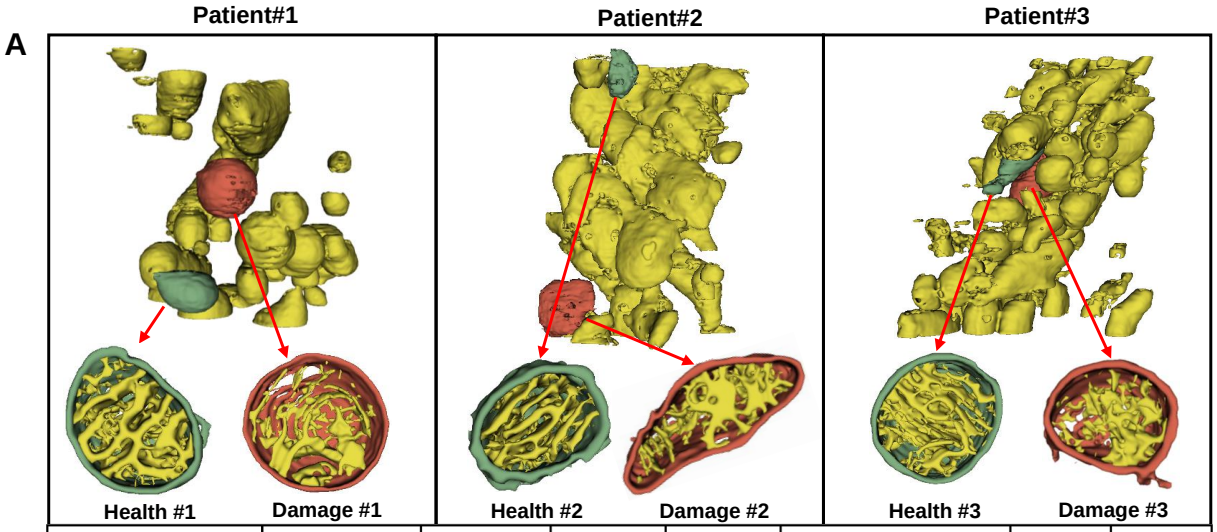


| Datasets | | Outer Membrane Surface(μm²) | Inner Cristae Surface(μm²) | Solid Volume(μm³) | Total Volume(μm³) | $S_{inner}/V_{total}$ (cristae density) (μm⁻¹) | $S_{inner}/S_{outer}$ (/) | $V_{solid}/V_{total}$ (/) |
|---|---|---|---|---|---|---|---|---|
| Patient#1 | Health #1 | 0.9569 | 4.0612 | 0.0693 | 0.1199 | **33.8628** | 4.2441 | 0.5776 |
| | Damage #1 | 2.1573 | 8.6646 | 0.1592 | 0.3801 | **22.7930** | 4.0163 | 0.4188 |
| Patient#2 | Health #2 | 1.0802 | 3.2176 | 0.0510 | 0.0858 | **37.4864** | 2.9787 | 0.5947 |
| | Damage #2 | 2.4705 | 8.6113 | 0.1372 | 0.2747 | **31.3417** | 3.4857 | 0.5000 |
| Patient#3 | Health #3 | 1.7026 | 8.7608 | 0.1143 | 0.2181 | **40.1636** | 5.1456 | 0.5241 |
| | Damage #3 | 1.7018 | 3.2842 | 0.0063 | 0.1277 | **25.7152** | 1.9299 | 0.5190 |

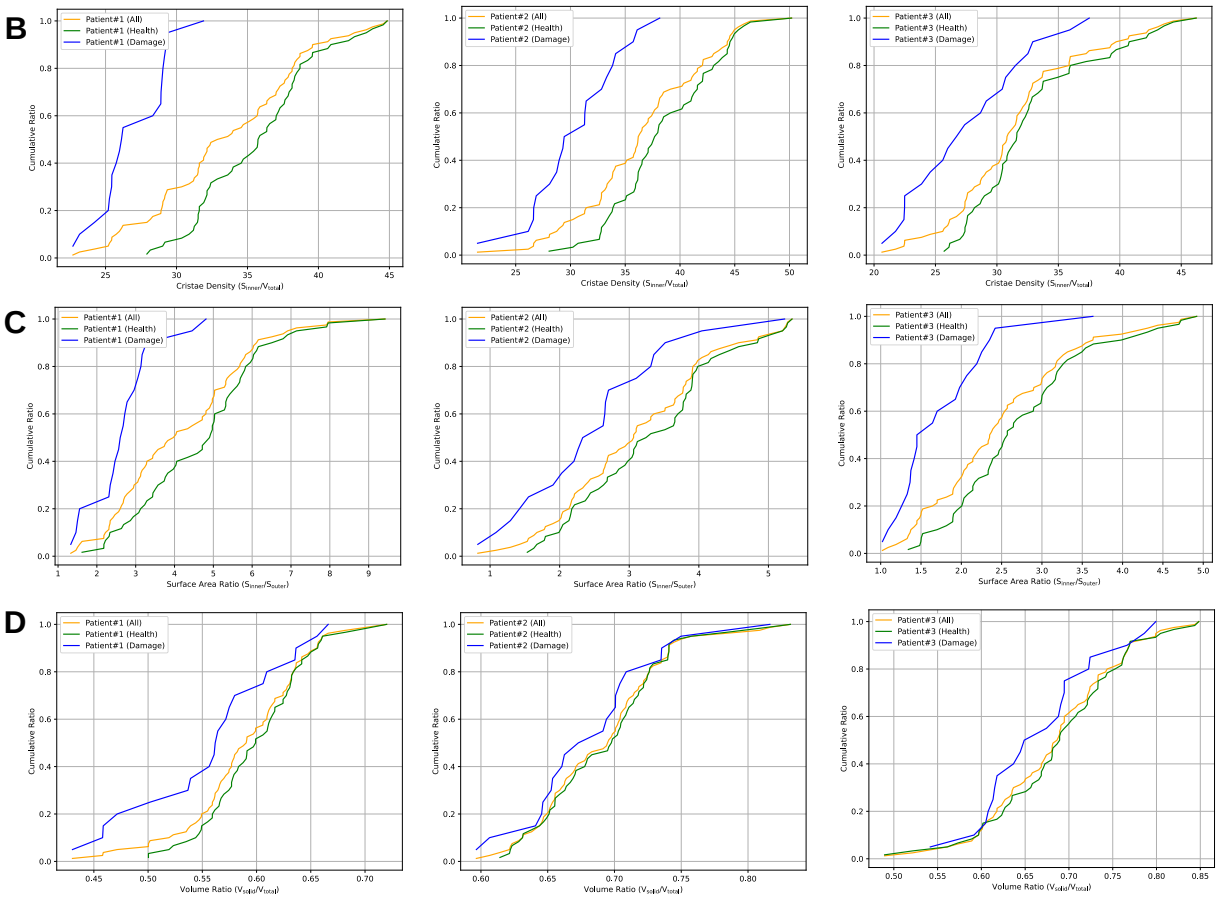


**Fig. 6 3D visualization and quantitative analysis of healthy and damaged mitochondria. A,** 3D visualization of segmentation results from three datasets, with green representing healthy mitochondrion and red representing damaged mitochondrion. Each dataset includes close-up views of one healthy and one damaged mitochondrion, along with quantitative data on outer membrane surface area, inner cristae surface area, solid volume, total volume, and calculated ratios ($S_{inner}/V_{total}$, $S_{inner}/S_{outer}$ and $V_{solid}/V_{total}$). **B,** Cumulative distribution plots of cristae density ($S_{inner}/V_{total}$) for each dataset. **C,** Cumulative distribution plots of the surface area ratio ($S_{inner}/S_{outer}$) for each dataset. **D,** Cumulative distribution plots of the volume ratio ($V_{solid}/V_{total}$) for each dataset. The blue, green, and orange lines in plots B, C, and D represent damaged, healthy, and all mitochondria, respectively. The three cumulative distribution plots demonstrate that the cumulative distributions of cristae density, surface area ratio, and volume ratio are lower for damaged mitochondria compared to healthy mitochondria, with the most notable difference observed in cristae density.

tion results, enabling a streamlined and efficient workflow for researchers.

## Discussion

In this study, we developed MitoStructSeg, a fully automated platform designed to overcome key challenges in both mitochondrial structure segmentation and quantitative analysis. The platform integrates two core modules: the mitochondrial structure segmentation module and the mitochondrial quantitative analysis module. The segmentation module employs the Adaptive Multi-Domain Mitochondrial Segmentation (AMM-Seg) method for accurate segmentation of mitochondrial structures, while the quantitative analysis module provides detailed metrics that are essential for understanding mitochondrial morphology and function.

Our results demonstrate that AMM-Seg significantly enhances segmentation accuracy for both the outer membrane and inner cristae, even when applied to datasets with limited or unlabeled data (Fig.3). This demonstrates the effectiveness of the multi-domain adaptation and adaptive fusion strategies, which enable robust and precise segmentation across diverse datasets. Furthermore, the quantitative analysis module in MitoStructSeg facilitates a comprehensive assessment of mitochondrial features, including surface area, volume, and cristae density, offering valuable insights into mitochondrial function (Fig.6).

Theoretically, MitoStructSeg advances the field by showcasing the synergy between mitochondrial structure segmentation and quantitative analysis in biomedical image processing. The AMM-Seg model offers novel insights into the segmentation of complex mitochondrial structures, while the quantitative analysis module delivers precise metrics for investigating mitochondrial morphology and function, thereby enhancing our understanding of the intricate relationship between structure and function. Practically, the platform has the potential to significantly impact biomedical research, particularly in the study of mitochondrial dysfunction and related diseases, where both structural and functional data are critical.

While MitoStructSeg represents a significant advancement, it has limitations that should be addressed in future research. Future work should focus on enhancing the model's self-learning capabilities, particularly by incorporating large-scale unlabeled datasets for training. Additionally, improving segmentation accuracy for mitochondrial structures by integrating more advanced feature extraction techniques and exploring the use of pretrained models tailored to specific domains will be essential to broaden its applicability.

In summary, MitoStructSeg makes a significant contribution to mitochondrial structure analysis by delivering superior segmentation accuracy and providing comprehensive quantitative analysis. Its robust performance across diverse datasets and ability to handle unlabeled data establish it as a powerful tool for mitochondrial research. By addressing both structural segmentation and quantitative analysis, this study lays the groundwork for future advancements in image analysis technologies and deep learning applications in biomedical research on mitochondrial dysfunction.

## Methods

### Section 1: Dataset Acquisition

In this study, we analyze the myocardial data of three male patients who underwent myocardial biopsy after COVID-19 infection to understand the health of the mitochondrial structure in their myocardium. Patient#1, 30 years old, underwent myocardial biopsy 37 days after infection and is diagnosed with viral myocarditis, sudden cardiac death, and ventricular fibrillation. Patient#2, 44 years old, underwent myocardial biopsy 58 days after infection and is diagnosed with viral myocarditis. Patient#3, 70 years old, underwent myocardial biopsy 76 days after infection and is diagnosed with viral myocarditis, atrial fibrillation, and personal history of cerebral infraction. By selecting these three patients, we obtain a rich data sample with a wide range of time spans and disease diversity, which provides important evidence for in-depth research on the impact of the disease on the myocardium and mitochondria.

The myocardial tissue samples are sourced from the three patients mentioned above, and the process for obtaining the data required for AI model training is as follows. Myocardial biopsy samples from COVID-19 patients are sectioned into 1x1 mm blocks and pre-fixed in a pH 7.2 solution containing 2% paraformaldehyde and 2.5% glutaraldehyde for 12 hours. The samples then underwent osmium-thiocarbohydrazide-osmium (OTO) staining. They are fixed in 1% osmium tetroxide with potassium ferrocyanide for 1 hour on ice, washed with phosphate buffer and ddH2O, treated with 1% thiocarbohydrazide, and post-fixed in 1% osmium tetroxide. Following staining with 1% uranium acetate and 0.66% lead citrate, the samples are dehydrated through a graded ethanol and acetone series, infiltrated with Epon 812 resin, and polymerized at 60°C for 48-72 hours. The resin blocks are observed under a dual-beam scanning electron microscope (Aquilos Cryo-FIB, Thermo Fisher Scientific). Each serial face is imaged using the T1 (in-lens detector) backscatter mode with an acceleration voltage of 2.0 keV and a current of 0.1 nA. Sequential milling is performed using a gallium ion beam, with a Z-axis height of 10 nm for each milling.

According to the above process, we obtain the data from three patients. The data sizes are 6144x4096x800 voxels for Patient#1, 6144x4096x800 voxels for Patient#2, and 6500x5200x800 voxels for Patient#3. The pixel size is 5x5 nm and the slice interval is 10 nm. Initially, we crop two regions (800x800x100 voxels) from

the data of Patient#1 and manually annotated them to create the source domain dataset (with labels). Subsequently, we crop a region (800x800x200 voxels) from the data of Patient#1, Patient#2, and Patient#3 respectively to form the target domain dataset (without labels). Additionally, we crop a region (800x800x40 voxels) from the data of these three patients to create the validation set for evaluating the segmentation accuracy and generalization performance of AMM-Seg.

**Section 2: AMM-Seg Model And Training**

The AMM-Seg model (Supplementary Fig.1) addresses mitochondrial segmentation challenges in noisy and complex imaging environments by leveraging a domain adaptation framework that minimizes labeling costs and improves model robustness. This framework uses both a labeled source domain and an unlabeled target domain, allowing for adaptive learning in the target domain and reducing dependency on manually labeled data. The core architecture of AMM-Seg is a dual-channel structure that extracts distinct image features, which are separated into augmented and textured features. An adaptive fusion module then integrates these features, enhancing segmentation accuracy for complex mitochondrial structure like cristae by preserving crucial texture details. To guide the model training across domains, we use specific loss functions, including a source domain segmentation loss, a target domain adaptation loss, and a domain classification loss. The following sections describe each module of the AMM-Seg model in detail.

**Dual-channel features Module**. To enhance generalization, reduce overfitting, and improve segmentation accuracy for fine mitochondrial structure such as cristae and membranes, we apply tailored data augmentation and texture extraction techniques to each domain. In the source domain, weak geometric augmentation ($\mathcal{A}_g$) prevents overfitting by applying transformations such as resizing, cropping, and flipping to generate augmented images, represented as $\boldsymbol{a}_i^S = \mathcal{A}_g(\boldsymbol{x}_i^S)$. For the target domain, random intensity-based augmentation ($\mathcal{A}_r$) is used to enhance robustness by varying contrast and brightness, resulting in $\boldsymbol{a}_i^T = \mathcal{A}_r(\boldsymbol{x}_i^T)$. Additionally, to capture essential texture details, we preprocess the images using a Gaussian blur to reduce noise and highlight significant structural patterns. Following this, a Canny edge detection filter is applied to extract image texture. This process generates texture-enhanced images, represented as $\boldsymbol{f}_i^S$ and $\boldsymbol{f}_i^T$ for the source and target domains, respectively. These preprocessing steps provide robust feature representations across diverse imaging conditions, facilitating accurate segmentation of intricate mitochondrial structure.

**Adaptive fusion Module**. For feature encoding, we employ the Cross-Slice Fusion (CSF) module to combine adjacent slices during downsampling, which retains continuity across the 2D mitochondrial slices. This operation is defined as:

$$\mathcal{D}_a^S = \text{Encoder}(\text{CSF}(\text{Encoder}(\boldsymbol{a}_i^S), \text{Encoder}(\boldsymbol{a}_{i+m}^S))), \tag{1}$$

$$\mathcal{D}_f^S = \text{Encoder}(\text{CSF}(\text{Encoder}(\boldsymbol{f}_i^S), \text{Encoder}(\boldsymbol{f}_{i+m}^S))). \tag{2}$$

where m=1, which means fusing adjacent images. And Encoder($\cdot$) represents the downsampling operation. CSF is applied to both augmented and texture-enhanced features, creating unified representations across adjacent slices. Similarly, for the target domain, we obtain $\mathcal{D}_a^T$ and $\mathcal{D}_f^T$.

To dynamically integrate encoding features, we design a channel adaptive fusion module inspired by the self-attention mechanism[43]. This module computes query, key, and value matrices $\boldsymbol{Q}^S$, $\boldsymbol{K}^S$, and $\boldsymbol{V}^S$ based on the channel attention representations of augmented and textured features, denoted as $h_a^S$ and $h_f^S$, as follows:

$$\boldsymbol{Q}^S, \boldsymbol{K}^S, \boldsymbol{V}^S = (W_q, W_k, W_v) \cdot [\boldsymbol{h}_a^S, \boldsymbol{h}_f^S], \tag{3}$$

$$\boldsymbol{h}_a^S, \boldsymbol{h}_f^S = \text{ChannelAtt}(\mathcal{D}_a^S, \mathcal{D}_f^S), \tag{4}$$

where $W_q$, $W_k$, and $W_v$ are learnable matrices. The fused representation $\boldsymbol{e}_i^S$ is then obtained by combining the encoded features with attention weights $\boldsymbol{w_a}$ and $\boldsymbol{w_f}$ as follows:

$$\boldsymbol{e}_i^S = (1 + \boldsymbol{w_a}) \cdot \mathcal{D}_a^S + (1 + \boldsymbol{w_f}) \cdot \mathcal{D}_f^S, \tag{5}$$

$$\boldsymbol{w_a}, \boldsymbol{w_f} = \text{MLP}(\text{softmax}(\frac{\boldsymbol{Q}^S(\boldsymbol{K}^S)^\top}{\sqrt{d_k}}) \cdot \boldsymbol{V}^S). \tag{6}$$

Similarly, we can obtain the encoding result $\boldsymbol{e}_i^T$ in the target domain. It is worth noting that the encoder of augmented and texture image features adopts a weight-sharing strategy to reduce model complexity and improve computational efficiency.

To effectively process segmentation and inter-slice variations, we employ a dual-decoder design. One decoder is dedicated to segmentation outputs (Equations (7) and (8)), while the other is designed to capture inter-slice variations (Equation (9). The Slice Decomposition (SD) module further separates adjacent slice features, defined as:

$$\boldsymbol{p}_i^S = \text{Decoder}(\text{SD}(\boldsymbol{e}_i^S, \text{Encoder}(\boldsymbol{a}_i^S), \text{Encoder}(\boldsymbol{f}_i^S))), \tag{7}$$

$$\boldsymbol{p}_{i+m}^S = \text{Decoder}(\text{SD}(\boldsymbol{e}_i^S, \text{Encoder}(\boldsymbol{a}_{i+m}^S), \text{Encoder}(\boldsymbol{f}_{i+m}^S))), \tag{8}$$

$$\boldsymbol{r}_i^S = \text{Decoder}(\boldsymbol{p}_i^S, \boldsymbol{p}_{i+m}^S), \tag{9}$$

where Decoder and $\text{Up}_{\text{diff}}$ are upsampling operations, but they differ in network structure. $\boldsymbol{p}_i^S$ and $\boldsymbol{p}_{i+m}^S$ is the segmentation result and $\boldsymbol{r}_i^S$ is the feature of image variation. Similarity allows us to obtain $\boldsymbol{p}_i^T$, $\boldsymbol{p}_{i+n}^T$, and $\boldsymbol{r}_i^T$ for the target domain.

**Loss Function**. To optimize segmentation quality and enable effective cross-domain adaptability, we design three types of loss functions: source domain loss, target domain loss, and domain classification loss.

The source domain loss ensures accurate segmentation in the labeled source domain through cross-entropy loss, addressing both segmentation performance and inter-slice continuity:

$$\mathcal{L}_{S1} = CE(\boldsymbol{p}_i^S, \boldsymbol{l}_i^S) + CE(\boldsymbol{p}_{i+1}^S, \boldsymbol{l}_{i+1}^S), \tag{10}$$

$$\mathcal{L}_{S2} = CE(\boldsymbol{r}_i^S, \mathrm{XOR}(\boldsymbol{l}_i^S, \boldsymbol{l}_{i+1}^S)), \tag{11}$$

where $CE(\cdot)$ represents cross-entropy loss, and $\mathrm{XOR}(\cdot)$ captures label differences between adjacent slices.

The target domain loss addresses the lack of labels in the target domain by generating pseudo-labels $\boldsymbol{l}_i^T$ and $\boldsymbol{l}_{i+1}^T$ from model predictions. Cross-entropy loss is computed for the target domain as follows:

$$\boldsymbol{l}_i^T = |\arg\max(\boldsymbol{p}_{i+1}^T) - \arg\max(\boldsymbol{r}_i^T)|, \tag{12}$$

$$\mathcal{L}_T = CE(\boldsymbol{p}_i^T, \boldsymbol{l}_i^T) + CE(\boldsymbol{p}_{i+1}^T, \boldsymbol{l}_{i+1}^T). \tag{13}$$

To achieve domain-invariant feature extraction, we use a domain classification loss with a gradient reversal layer (GRL)[44], guiding a domain classifier to differentiate between source and target domain data:

$$d_i^S, d_i^T = G_d(\mathrm{GRL}(\boldsymbol{e}_i^S, \boldsymbol{e}_i^T)), \tag{14}$$

$$\mathcal{L}_C = CE(\boldsymbol{d}_i^S, d_i'^S) + CE(\boldsymbol{d}_i^T, d_i'^T), \tag{15}$$

where $G_d$ is domain classification function, $d_i'^S$ and $d_i'^T$ are the domain labels.

The total loss function, $\mathcal{L}$, combines these three loss components, with $\lambda_1$ and $\lambda_2$ controlling the contributions of target domain loss and domain classification loss, respectively:

$$\mathcal{L} = \mathcal{L}_{S1} + \mathcal{L}_{S2} + \lambda_1 \mathcal{L}_T + \lambda_2 \mathcal{L}_C. \tag{16}$$

**Training details.** The training process begins with an initial learning rate of 0.0005, which is dynamically adjusted throughout the training period using a polynomial decay strategy with a decay power of 0.9. This strategy reduces the learning rate progressively over a total of 10,000 iterations, promoting stable convergence and helping to prevent early overfitting. The optimization is conducted using the Adam optimizer[45], configured with $\beta_1 = 0.9$ and $\beta_2 = 0.99$. A batch size of 2 is employed, with a random selection of samples at each iteration. Given this batch size, the model completes a total of 10,000 effective iterations across the dataset. The parameters of the loss function, as specified in Equation (16), are consistently set to $\lambda_1 = 0.1$ and $\lambda_2 = 0.1$. For uniformity and comparability across experiments, the configuration settings—including optimizer parameters, learning rate schedule, batch size, and loss weights—are kept identical for each of the three datasets used in the training process.

## Section 3: Other Supplementary

**Code avalidability.** The AMM-Seg segmentation algorithms are trained using pytorch 2.4.1, and the quantification algorithms are implemented in Python 3.8.19 using the libraries: albumentations 1.4.7, numpy 1.24.4, opencv-python 4.9.0.80, scikit-image 0.21.0, scipy 1.10.1, and pandas 2.0.3. These algorithms are accelerated using the GPUs (NVIDIA A100-PCIE-40GB) on CentOS Linux 7. The GUI is built using React 18.3.1 and Vite 5.2.10, integrated with Ant Design 5.19.3 and Material UI component libraries to provide a modern user interface and responsive layout. The project is developed using Node.js 18.17.1 and JavaScript, with all dependencies managed through npm 9.6.7. The data visualization section incorporates Chart.js 4.4.3, Echarts 5.5.1, and ApexCharts 3.46.2, supporting dynamic display of various types of charts. Additional details, source code, and documentation are available at: https://github.com/xiaohuawan/MitoStructSeg.

**3D visualization.** 3D visualization of mitochondrial structure is performed using 3D Slicer version 5.6.2[36].

### References


[1] Marta Giacomello, Aswin Pyakurel, Christina Glytsou, and Luca Scorrano. The cell biology of mitochondrial membrane dynamics. *Nature reviews Molecular cell biology*, 21 (4):204–224, 2020.

[2] Gulcin Pekkurnaz and Xinnan Wang. Mitochondrial heterogeneity and homeostasis through the lens of a neuron. *Nature metabolism*, 4(7):802–812, 2022.

[3] Lena Pernas and Luca Scorrano. Mito-morphosis: mitochondrial fusion, fission, and cristae remodeling as key mediators of cellular function. *Annual review of physiology*, 78(1):505–531, 2016.

[4] Florian J Bock and Stephen WG Tait. Mitochondria as multifaceted regulators of cell death. *Nature reviews Molecular cell biology*, 21(2):85–100, 2020.

[5] Anna Picca, Riccardo Calvani, Hélio José Coelho-Junior, and Emanuele Marzetti. Cell death and inflammation: The role of mitochondria in health and disease. *Cells*, 10(3):537, 2021.

[6] Esmee Vringer and Stephen WG Tait. Mitochondria and cell death-associated inflammation. *Cell Death & Differentiation*, 30(2):304–312, 2023.

[7] Zahra Al Amir Dache and Alain R Thierry. Mitochondria-derived cell-to-cell communication. *Cell Reports*, 42(7), 2023.

[8] Yansheng Feng, Abdulhafiz Imam Aliagan, Nathalie Tombo, and Jean C Bopassa. Mitofilin heterozygote mice display an increase in myocardial injury and inflammation after ischemia/reperfusion. *Antioxidants*, 12(4):921, 2023.

[9] Patricia Sánchez-Pérez, Ana Mata, May-Kristin Torp, Elia López-Bernardo, Christina M Heiestad, Jan Magnus Aronsen, Antonio Molina-Iracheta, Luis J Jiménez-Borreguero, Pablo García-Roves, Ana SH Costa, et al. Energy substrate metabolism, mitochondrial structure and oxidative

stress after cardiac ischemia-reperfusion in mice lacking ucp3. *Free Radical Biology and Medicine*, 205:244–261, 2023.

[10] Sabzali Javadov, Andrey V Kozlov, and Amadou KS Camara. Mitochondria in health and diseases, 2020.

[11] Giacomo Monzio Compagnoni, Alessio Di Fonzo, Stefania Corti, Giacomo P Comi, Nereo Bresolin, and Eliezer Masliah. The role of mitochondria in neurodegenerative diseases: the lesson from alzheimer's disease and parkinson's disease. *Molecular neurobiology*, 57:2959–2980, 2020.

[12] Andrea G Marshall, Steven M Damo, and Antentor Hinton. Revisiting focused ion beam scanning electron microscopy. *Trends in Biochemical Sciences*, 48(6):585–586, 2023.

[13] Tanmoy Saha, Chinmayee Dash, Ruparoshni Jayabalan, Sachin Khiste, Arpita Kulkarni, Kiran Kurmi, Jayanta Mondal, Pradip K Majumder, Aditya Bardia, Hae Lin Jang, et al. Intercellular nanotubes mediate mitochondrial trafficking between cancer and immune cells. *Nature nanotechnology*, 17(1):98–106, 2022.

[14] Nicholas Borcherding and Jonathan R Brestoff. The power and potential of mitochondria transfer. *Nature*, 623(7986): 283–291, 2023.

[15] C Shan Xu, Song Pang, Gleb Shtengel, Andreas Müller, Alex T Ritter, Huxley K Hoffman, Shin-ya Takemura, Zhiyuan Lu, H Amalia Pasolli, Nirmala Iyer, et al. An open-access volume electron microscopy atlas of whole cells and tissues. *Nature*, 599(7883):147–151, 2021.

[16] Stefan Stoldt, Till Stephan, Daniel C Jans, Christian Brüser, Felix Lange, Jan Keller-Findeisen, Dietmar Riedel, Stefan W Hell, and Stefan Jakobs. Mic60 exhibits a coordinated clustered distribution along and across yeast and mammalian mitochondria. *Proceedings of the National Academy of Sciences*, 116(20):9853–9858, 2019.

[17] Stefan Stoldt, Dirk Wenzel, Kirsten Kehrein, Dietmar Riedel, Martin Ott, and Stefan Jakobs. Spatial orchestration of mitochondrial translation and oxphos complex assembly. *Nature cell biology*, 20(5):528–534, 2018.

[18] Till Stephan, Christian Brüser, Markus Deckers, Anna M Steyer, Francisco Balzarotti, Mariam Barbot, Tiana S Behr, Gudrun Heim, Wolfgang Hübner, Peter Ilgen, et al. Micos assembly controls mitochondrial inner membrane remodeling and crista junction redistribution to mediate cristae formation. *The EMBO journal*, 39(14):e104105, 2020.

[19] Sergio A Muñoz-Gómez, Lawrence Rudy Cadena, Alastair T Gardiner, Michelle M Leger, Shaghayegh Sheikh, Louise B Connell, Tomáš Bilỳ, Karel Kopejtka, J Thomas Beatty, Michal Koblížek, et al. Intracytoplasmic-membrane development in alphaproteobacteria involves the homolog of the mitochondrial crista-developing protein mic60. *Current Biology*, 33(6):1099–1111, 2023.

[20] Arun Kumar Kondadi, Ruchika Anand, and Andreas S Reichert. Cristae membrane dynamics–a paradigm change. *Trends in cell biology*, 30(12):923–936, 2020.

[21] Chenguang Wang, Masayasu Taki, Yoshikatsu Sato, Yasushi Tamura, Hideyuki Yaginuma, Yasushi Okada, and Shigehiro Yamaguchi. A photostable fluorescent marker for the superresolution live imaging of the dynamic structure of the mitochondrial cristae. *Proceedings of the National Academy of Sciences*, 116(32):15817–15822, 2019.

[22] Mayuko Segawa, Dane M Wolf, Nan W Hultgren, David S Williams, Alexander M van der Bliek, David B Shackelford, Marc Liesa, and Orian S Shirihai. Quantification of cristae architecture reveals time-dependent characteristics of individual mitochondria. *Life science alliance*, 3(7), 2020.

[23] Xiaoshuai Huang, Junchao Fan, Liuju Li, Haosen Liu, Runlong Wu, Yi Wu, Lisi Wei, Heng Mao, Amit Lal, Peng Xi, et al. Fast, long-term, super-resolution imaging with hessian structured illumination microscopy. *Nature biotechnology*, 36(5):451–459, 2018.

[24] Chao Hu, Li Shu, Xiaoshuai Huang, Jianglong Yu, Liuju Li, Longlong Gong, Meigui Yang, Zhida Wu, Zhi Gao, Yungang Zhao, et al. Opa1 and micos regulate mitochondrial crista dynamics and formation. *Cell death & disease*, 11 (10):940, 2020.

[25] Amy E Vincent, Kathryn White, Tracey Davey, Jonathan Philips, R Todd Ogden, Conor Lawless, Charlotte Warren, Matt G Hall, Yi Shiau Ng, Gavin Falkous, et al. Quantitative 3d mapping of the human skeletal muscle mitochondrial network. *Cell reports*, 26(4):996–1009, 2019.

[26] Chenhao Wang, Leif Østergaard, Stine Hasselholt, and Jon Sporring. A semi-automatic method for extracting mitochondrial cristae characteristics from 3d focused ion beam scanning electron microscopy data. *Communications Biology*, 7(1):377, 2024.

[27] Pengshuai Yin, Rui Yuan, Yiming Cheng, and Qingyao Wu. Deep guidance network for biomedical image segmentation. *IEEE access*, 8:116106–116116, 2020.

[28] Philipp D Lösel, Thomas van de Kamp, Alejandra Jayme, Alexey Ershov, Tomáš Faragó, Olaf Pichler, Nicholas Tan Jerome, Narendar Aadepu, Sabine Bremer, Suren A Chilingaryan, et al. Introducing biomedisa as an open-source online platform for biomedical image segmentation. *Nature communications*, 11(1):5577, 2020.

[29] Kévin Cortacero, Brienne McKenzie, Sabina Müller, Roxana Khazen, Fanny Lafouresse, Gaëlle Corsaut, Nathalie Van Acker, François-Xavier Frenois, Laurence Lamant, Nicolas Meyer, et al. Evolutionary design of explainable algorithms for biomedical image segmentation. *Nature communications*, 14(1):7112, 2023.

[30] Liqing Liu, Shuxin Yang, Yang Liu, Xixia Li, Junjie Hu, Li Xiao, and Tao Xu. Deepcontact: High-throughput quantification of membrane contact sites based on electron microscopy imaging. *Journal of Cell Biology*, 221(9): e202106190, 2022.

[31] Olaf Ronneberger, Philipp Fischer, and Thomas Brox. U-net: Convolutional networks for biomedical image segmentation. In *Medical image computing and computer-assisted intervention–MICCAI 2015: 18th international conference, Munich, Germany, October 5-9, 2015, proceedings, part III 18*, pages 234–241. Springer, 2015.

[32] Shogo Suga, Koki Nakamura, Yu Nakanishi, Bruno M Humbel, Hiroki Kawai, and Yusuke Hirabayashi. An interactive deep learning-based approach reveals mitochondrial cristae topologies. *PLoS Biology*, 21(8):e3002246, 2023.

[33] Gihun Lee, SangMook Kim, Joonkee Kim, and Se-Young Yun. Mediar: Harmony of data-centric and model-centric for multi-modality microscopy. *arXiv preprint arXiv:2212.03465*, 2022.

[34] Jun Ma, Ronald Xie, Shamini Ayyadhury, Cheng Ge, Anubha Gupta, Ritu Gupta, Song Gu, Yao Zhang, Gihun Lee, Joonkee Kim, et al. The multimodality cell segmentation challenge: toward universal solutions. *Nature methods*, pages 1–11, 2024.

[35] Wei Huang, Xiaoyu Liu, Zhen Cheng, Yueyi Zhang, and Zhiwei Xiong. Domain adaptive mitochondria segmen-

tation via enforcing inter-section consistency. In *International Conference on Medical Image Computing and Computer-Assisted Intervention*, pages 89–98. Springer, 2022.

[36] Andriy Fedorov, Reinhard Beichel, Jayashree Kalpathy-Cramer, Julien Finet, Jean-Christophe Fillion-Robin, Sonia Pujol, Christian Bauer, Dominique Jennings, Fiona Fennessy, Milan Sonka, et al. 3d slicer as an image computing platform for the quantitative imaging network. *Magnetic resonance imaging*, 30(9):1323–1341, 2012.

[37] Ali Hatamizadeh, Vishwesh Nath, Yucheng Tang, Dong Yang, Holger R Roth, and Daguang Xu. Swin unetr: Swin transformers for semantic segmentation of brain tumors in mri images. In *International MICCAI brainlesion workshop*, pages 272–284. Springer, 2021.

[38] Ali Hatamizadeh, Yucheng Tang, Vishwesh Nath, Dong Yang, Andriy Myronenko, Bennett Landman, Holger R Roth, and Daguang Xu. Unetr: Transformers for 3d medical image segmentation. In *Proceedings of the IEEE/CVF winter conference on applications of computer vision*, pages 574–584, 2022.

[39] Claude E Duchon. Lanczos filtering in one and two dimensions. *Journal of Applied Meteorology and Climatology*, 18 (8):1016–1022, 1979.

[40] George Law. Quantitative comparison of flood fill and modified flood fill algorithms. *International Journal of Computer Theory and Engineering*, 5(3):503–508, 2013.

[41] Raquel A Adams, Zheng Liu, Chongere Hsieh, Michael Marko, W Jonathan Lederer, M Saleet Jafri, and Carmen Mannella. Structural analysis of mitochondria in cardiomyocytes: insights into bioenergetics and membrane remodeling. *Current Issues in Molecular Biology*, 45(7):6097–6115, 2023.

[42] Joachim Nielsen, Kasper D Gejl, Martin Hey-Mogensen, Hans-Christer Holmberg, Charlotte Suetta, Peter Krustrup, Coen PH Elemans, and Niels Ørtenblad. Plasticity in mitochondrial cristae density allows metabolic capacity modulation in human skeletal muscle. *The Journal of physiology*, 595(9):2839–2847, 2017.

[43] Ashish Vaswani, Noam Shazeer, Niki Parmar, Jakob Uszkoreit, Llion Jones, Aidan N Gomez, Łukasz Kaiser, and Illia Polosukhin. Attention is all you need. *Advances in neural information processing systems*, 30, 2017.

[44] Yaroslav Ganin and Victor Lempitsky. Unsupervised domain adaptation by backpropagation. In *International conference on machine learning*, pages 1180–1189. PMLR, 2015.

[45] Diederik P Kingma and JL Ba. Adam: A method for stochastic optimization 3rd international conference on learning representations. In *ICLR 2015-Conference Track Proceedings*, volume 1, 2015.